

Revealing the Reaction Mechanism of C-C Coupling on Cu-based Tandem Catalysts towards CO₂ Reduction

Xiangdong Kong

University of Science and Technology of China

Jingwen Ke

University of Science and Technology of China

Weiran Zhou

University of Science and Technology of China

Zhengwu Yang

University of Science and Technology of China

Mingfang Chi

University of Science and Technology of China

Cheng Wang

University of Science and Technology of China

Sijia Li

University of Science and Technology of China

Rui Si

Shanghai Institute of Applied Physics

Bin Liu

Nanyang Technological University <https://orcid.org/0000-0002-4685-2052>

Zhigang Geng

University of Science and Technology of China

Jie Zeng (✉ zengj@ustc.edu.cn)

University of Science and Technology of China <https://orcid.org/0000-0002-8812-0298>

Article

Keywords: tandem mechanism, *CO coverage, C₂+ products, CO₂ electroreduction

Posted Date: December 7th, 2020

DOI: <https://doi.org/10.21203/rs.3.rs-115130/v1>

License: © ⓘ This work is licensed under a Creative Commons Attribution 4.0 International License.

[Read Full License](#)

Abstract

Cu-based tandem catalysts have widely been exploited to improve the catalytic performance for multi-carbon (C₂₊) products towards CO₂ electroreduction. Nevertheless, the underlying reaction mechanism for tandem catalytic system remains ambiguity. Herein, we unraveled the relationship between the behavior of adsorbed CO intermediate (*CO) and the process of C-C coupling. Due to the low coverage of *CO, the process of C-C coupling has always been restricted for Cu catalysts. Through regulating the molar ratios of CO₂ to CO in co-feeding gases, we found that the moderate surface coverage of *CO was beneficial for the electroreduction of CO₂ into ethylene (C₂H₄). Meanwhile, the cross-coupling process between CO₂ and CO was proved to be responsible for the enhanced activity of C₂H₄ according to isotopic labeling experiments. We constructed a tandem model with cobalt phthalocyanine (CoPc) as CO-generating component on Cu to further verify the tandem mechanism. With the introduction of CoPc onto the surface of Cu, the partial current density for C₂H₄ reached as high as 313 mA cm⁻² at applied current density of 480 mA cm⁻², which was one-fold higher than that (165 mA cm⁻²) of Cu film. In-situ Raman measurements further revealed that CO generated by CoPc increased the coverage of *CO on the surface of Cu, facilitating the process of C-C coupling.

Introduction

The excessive utilization of fossil fuels emits a large amount of CO₂, giving rise to energy shortage and environmental crisis¹⁻⁵. To meet the ever-increasing energy demands and to mitigate ever-fragile environmental status, researchers have exploited a series of strategies such as chemical reforming^{6,7}, photoreduction^{8,9}, biological conversion^{10,11}, and electroreduction¹²⁻¹⁶ *via* transforming CO₂ into useful chemicals and feedstocks. Among these strategies, CO₂ electroreduction, which operates under ambient pressure at room temperature, serves as one of the promising ways to promote CO₂ utilization and global carbon recycling¹⁷⁻²¹. During the process of CO₂ electroreduction, a variety of carbonaceous products, including carbon monoxide (CO), formate (HCOO⁻), methane (CH₄), ethylene (C₂H₄), propylene (C₃H₆), ethanol (C₂H₅OH), and acetate (CH₃COO⁻) have been reported²²⁻²⁴. Especially, multi-carbon (C₂₊) products have been widely used as key feedstocks for industrial manufacture and liquid fuels due to their unique chemical functional groups and high energy density²⁵. As such, it is of pivotal significance to construct the highly efficient electrocatalysts for C₂₊ products towards CO₂ electroreduction.

Among all catalysts, Cu-based nanocrystals have been regarded as the most efficient catalysts to generate C₂₊ products towards CO₂ electroreduction. Great efforts have been devoted to improve the selectivity for C₂₊ products *via* engineering active phases²⁶⁻²⁸ and constructing compositions²⁹⁻³². In addition, the strategy for designing tandem catalysts where Cu-based nanocrystals coupled with CO-generating catalysts have been considered as the most effective method to improve catalytic performance for C₂₊ products. Up till now, a series of Cu-based tandem catalysts including Cu₄Zn³³, Ag-Cu₂O_{PB}³⁴, Au/Cu bimetallic³⁵, Cu dots on Ag substrate³⁶, Cu-Ag bimetallic²⁵, CuO_x/NiNC³⁷, and Cu/Zn

bimetallic³⁸ have been developed for CO₂ electroreduction into C₂₊ products. Despite all those achievements, the underlying reaction mechanism for tandem catalytic system remains ambiguity. Therefore, the understanding of the intrinsic reaction mechanism for tandem catalysts is of great importance to design efficient catalysts for the electroreduction of CO₂ into C₂₊ products.

Herein, we unraveled the relationship between the behavior of adsorbed CO intermediate (*CO) and the process of C-C coupling. Due to the low coverage of *CO, the process of C-C coupling has always been restricted for Cu catalysts. Through regulating the molar ratios of CO₂ to CO in co-feeding gases, we found that the moderate surface coverage of *CO was beneficial for the electroreduction of CO₂ into C₂H₄. Meanwhile, the cross-coupling process between CO₂ and CO was proved to be responsible for the enhanced activity of C₂H₄ according to isotopic labeling experiments. We constructed a tandem model with cobalt phthalocyanine (CoPc) as CO-generating component on Cu to further verify the tandem mechanism. With the introduction of CoPc onto the surface of Cu, the partial current density for C₂H₄ reached as high as 313 mA cm⁻² at applied current density (*j*) of 480 mA cm⁻², which was one-fold higher than that (165 mA cm⁻²) of Cu film. *In-situ* Raman measurements further revealed that CO generated by CoPc increased the coverage of *CO on the surface of Cu, facilitating the process of C-C coupling.

Results

Synthesis and structural characterizations of gas diffusion electrode (GDE) of Cu. The GDE of Cu was prepared *via* sputtering Cu on the porous polytetrafluoroethylen (PTFE) frames. As shown in scanning electron microscopy (SEM) images, Cu film was uniformly coated on the PTFE (Fig. 1a and b). Fig. 1c shows the high-angle annular dark field scanning transmission electron microscopy (HAADF-STEM) image of Cu nanocrystal. The interplanar spacings of 0.205 and 0.181 nm were assigned to (111) and (200) facets of face-centered-cubic (*fcc*) Cu, respectively. The single-crystal structure of Cu nanocrystal was identified by the selected area electron diffraction (SAED) pattern (Fig. 1c, inset). Fig. 1d shows X-ray diffraction (XRD) patterns of PTFE and the GDE of Cu. Except for the characteristic peaks for PTFE, other peaks located at 43.3°, 50.4°, and 74.1° for the GDE of Cu were indexed to the (111), (200), and (220) facets of *fcc* Cu (JCPDS No. 04-0836), respectively. We further investigated the valence state of Cu in the GDE of Cu. As shown in Fig. 1e, a characteristic peak at 918.8 eV was observed in the Cu *LMM* Auger spectrum, demonstrating the metallic Cu species in the GDE of Cu. Fig. 1f shows the *K*-edge X-ray absorption near-edge spectroscopy (XANES) spectra of Cu foil, Cu₂O, and GDE of Cu. The GDE of Cu exhibited a similar energy absorption edge profile with Cu foil in the range between 8970.0 and 9000.0 eV. Moreover, the first-order derivative peak of XANES profile for the GDE of Cu was located at 8979.0 eV, further revealing the metallic state of Cu in the GDE of Cu (Supplementary Fig. 1).

To improve structural stability for the GDE of Cu, we constructed a hydrophobic layer *via* spraying carbon black (Vulcan, XC-72) on Cu film³⁹⁻⁴¹. After spraying a layer of carbon black onto Cu film, the GDE of Cu was regulated from hydrophilic to hydrophobic with the contact angles increased from 65.5° to 121.5°

(Fig. 1g). As shown in Fig. 1h, the average thickness of Cu film and carbon black in the GDE of Cu were about 0.6 and 1.5 μm , respectively. The structure for the GDE of Cu was further proved by energy dispersive X-ray (EDX) elemental mapping with clear contrasts among carbon black, Cu film, and PTFE frames (Fig. 1i).

Catalytic performance for the GDE of Cu towards CO_2 electroreduction. A flow-cell system with 1 M KOH as electrolyte was used to evaluate the catalytic performance for the GDE of Cu (Supplementary Fig. 2). During the process of chronopotentiometric electrolysis, the gaseous products including hydrogen (H_2), CO, CH_4 , C_2H_4 , and C_3H_6 were quantified *via* online gas chromatography (GC) (Supplementary Fig. 3). Meanwhile, the liquid products containing HCOO^- , $\text{C}_2\text{H}_5\text{OH}$, and CH_3COO^- were quantitatively analyzed *via* ^1H nuclear magnetic resonance (^1H NMR) (Supplementary Figs. 4 and 5). As shown in Fig. 2a, a volcano-type behavior between faradaic efficiency (FE) for C_2H_4 ($\text{FE}_{\text{C}_2\text{H}_4}$) and applied j was observed for the GDE of Cu. At applied j of 300 mA cm^{-2} , the GDE of Cu achieved the highest $\text{FE}_{\text{C}_2\text{H}_4}$ of 43%. The other C_{2+} products such as $\text{C}_2\text{H}_5\text{OH}$, CH_3COOH , and C_3H_6 were also generated during CO_2 electroreduction (Supplementary Fig. 6). Apart from the C_{2+} products, the GDE of Cu also exhibited a relatively steady FE for HCOO^- ($\text{FE}_{\text{HCOO}^-}$) of about 15% and FE for CH_4 (FE_{CH_4}) of around 2% at all applied j (Supplementary Fig. 7). Fig. 2b shows the FE for CO (FE_{CO}). FE_{CO} decreased with the increase of applied j . When the applied j was higher than 360 mA cm^{-2} , FE_{CO} was limited within 3%. As shown in Fig. 2c, the highest j for C_2H_4 ($j_{\text{C}_2\text{H}_4}$) was 165 mA cm^{-2} at applied j of 480 mA cm^{-2} . Nevertheless, j for CO (j_{CO}) decreased with the increased tendency of $j_{\text{C}_2\text{H}_4}$ (Fig. 2d). A reasonable explanation for this phenomenon is that $^*\text{CO}$ is the essential intermediate for the formation of C_2H_4 .

The investigation of tandem mechanism for the GDE of Cu. To gain insight into the C-C coupling mechanism for the formation of C_2H_4 , we monitored the $\text{FE}_{\text{C}_2\text{H}_4}$ for the GDE of Cu at applied j of 300 mA cm^{-2} with various partial pressures of CO_2 and CO as co-feeding gases. As shown in Fig. 3a, the GDE of Cu exhibited a volcano-type relationship between $\text{FE}_{\text{C}_2\text{H}_4}$ and partial pressure of gaseous CO. When the partial pressure of CO reached 8%, the GDE of Cu displayed the highest $\text{FE}_{\text{C}_2\text{H}_4}$ of 59%, which was 1.4 times as high as the GDE of Cu with pure CO_2 as feeding gas (43%). We deduced that the enhanced $\text{FE}_{\text{C}_2\text{H}_4}$ was attributed to the increased surface coverage of $^*\text{CO}$ which originated from the increased partial pressure of gaseous CO. Further increasing the partial pressure of CO to 16% led to the decrease of $\text{FE}_{\text{C}_2\text{H}_4}$. To unravel the role of gaseous CO in the formation of C_2H_4 , we adopted isotopic labeling experiments using $^{13}\text{CO}_2$ and CO as co-feeding gas ($^{13}\text{CO}_2:\text{CO}=92:8$). At applied j of 300 mA cm^{-2} , C_2H_4 -correlated fragments were quantitatively analyzed by gas chromatography-mass spectrometer (GC-MS) measurements over the GDE of Cu. The calibrations and ratios of C_2H_4 -correlated fragments

were shown in Supplementary Fig. 8 and Supplementary Table 1. To exclude the influence of CO-correlated fragments (^{13}CO with m/z of 29 and CO with m/z of 28), we chose the mass spectrometry signals with m/z of 30, 27, and 26 to quantitatively analyze the ratios for $^{13}\text{C}_2\text{H}_4$, $^{13}\text{CH}_2\text{CH}_2$, and C_2H_4 . According to the quantitative equations and the peak areas of fragments with m/z of 30, 27, and 26, the ratios for $^{13}\text{C}_2\text{H}_4$, $^{13}\text{CH}_2\text{CH}_2$, and C_2H_4 were calculated to be 57.1%, 42.5%, and 0.4%, respectively (Fig. 3b). The abundant product of $^{13}\text{CH}_2\text{CH}_2$ proved that the cross-coupling process proceeded between CO_2 and CO .

To investigate the interferences of the local pH of electrolyte around the surface of catalysts and partial pressure of gaseous CO_2 , we conducted CO_2 electroreduction over the GDE of Cu using CO_2 and Ar as co-feeding gases at applied j of 300 mA cm^{-2} . As shown in Fig. 3c, a relatively steady $\text{FE}_{\text{C}_2\text{H}_4}$ of 40% was acquired for the GDE of Cu as the partial pressure of CO_2 ranged from 100% to 84%. This result indicated that the enhanced $\text{FE}_{\text{C}_2\text{H}_4}$ in the co-feeding gases of CO_2 and CO was not ascribed to the increased local pH. In addition, the $\text{FE}_{\text{C}_2\text{H}_4}$ gradually decreased as the partial pressure of CO_2 decreased from 70% to 10% using CO_2 and Ar as co-feeding gases (Supplementary Fig. 9). The decreased $\text{FE}_{\text{C}_2\text{H}_4}$ could be attributed to the low partial pressure of gaseous CO_2 which hindered the kinetic process for the formation of $^*\text{CO}$ and thus the coupling process of $^*\text{CO}$ into $^*\text{OCCO}$. To verify whether the enhanced $\text{FE}_{\text{C}_2\text{H}_4}$ was originated from the coupling process of CO , we conducted CO electroreduction in various co-feeding gases of Ar and CO at applied j of 300 mA cm^{-2} . When partial pressure of CO ranged from 0% to 16%, $\text{FE}_{\text{C}_2\text{H}_4}$ gradually increased from 0% to 4% (Fig. 3d). Nevertheless, when the partial pressure of CO was further increased from 30% to 90%, all of the $\text{FE}_{\text{C}_2\text{H}_4}$ for the GDE of Cu remained around 4% (Supplementary Fig. 10). Especially, when pure CO served as feeding gas, $\text{FE}_{\text{C}_2\text{H}_4}$ was still less than 5% as applied j was higher than 300 mA cm^{-2} (Supplementary Fig. 11). The poor catalytic activity for CO electroreduction into C_2H_4 could be ascribed to the overloaded coverage of $^*\text{CO}$ on Cu surface. The overloaded coverage of $^*\text{CO}$ restricts the coverage of $^*\text{H}$, depressing the hydrogenation kinetics of $^*\text{OCCO}$ to $^*\text{OCCOH}$ ^{36,42}. As a consequence, we concluded that a moderate coverage of $^*\text{CO}$ was beneficial for the formation of C_2H_4 .

To validate the tandem process between CO_2 and CO , we constructed a type of tandem catalyst *via* coupling CoPc with the GDE of Cu (denoted as Cu-CoPc). In these tandem catalysts, the electronic structure of Cu maintained original state due to the van der Waals contact between CoPc and Cu, in which CoPc served as highly efficient catalyst for the formation of CO .⁴³ Notably, CoPc exhibited remarkable catalytic performance in flow-cell system with FE_{CO} higher than 90% in a wide region of applied j from 60 to 360 mA cm^{-2} (Supplementary Fig. 12). To explore the matched degree between CoPc and Cu, we prepared a series of tandem catalysts by spraying different amount of CoPc onto Cu film. The compositions of Cu-CoPc were investigated by Raman spectra. As shown in the Supplementary Fig. 13, all of the Cu-CoPc catalysts exhibited the obvious peaks at 681.9, 1337.2, and 1537.9 cm^{-1} , which were attributed to the characteristic peaks for CoPc. In addition, the intensity of the characteristic peaks for the four Cu-CoPc catalysts gradually increased associated with the increased contents of CoPc. Determined

by the inductively coupled plasma atomic emission spectroscopy (ICP-AES), the molar ratios of CoPc to Cu were 3.1%, 6.2%, 10.4%, and 16.6%, denoting these samples as Cu-CoPc-1, Cu-CoPc-2, Cu-CoPc-3, and Cu-CoPc-4, respectively (Supplementary Table 2). Supplementary Fig. 14 shows the EDX elemental mapping of the four Cu-CoPc catalysts, where Co and N uniformly distributed on the GDE of Cu.

To evaluate the catalytic performance of these tandem catalysts, we conducted chronopotentiometric electrolysis. As shown in Fig. 4a and Supplementary Fig. 15, Cu-CoPc-2 achieved the highest $FE_{C_2^+}$ of 82% at applied j of 480 mA cm^{-2} , which was 1.4, 1.2, and 2.0 times as high as Cu-CoPc-1 (57%), Cu-CoPc-3 (70%), and Cu-CoPc-4 (41%) under the similar applied potentials, respectively. Fig. 4b shows the $FE_{C_2H_4}$ for the four Cu-CoPc catalysts. As the applied j ranging from 240 to 480 mA cm^{-2} , Cu-CoPc-2 always exhibited the highest $FE_{C_2H_4}$ among all of the Cu-CoPc catalysts. When applied j was set at 420 mA cm^{-2} , the $FE_{C_2H_4}$ of Cu-CoPc-2 was up to 67%, which was 1.3, 1.1, and 1.6 times as high as those of Cu-CoPc-1 (50%), Cu-CoPc-3 (60%), and Cu-CoPc-4 (42%), respectively. Fig. 4c shows the $j_{C_2H_4}$ for the four Cu-CoPc catalysts. Cu-CoPc-2 also exhibited the highest $j_{C_2H_4}$ with respect to the other counterparts at the applied j ranging from 240 to 480 mA cm^{-2} . Especially, at the applied j of 480 mA cm^{-2} , the $j_{C_2H_4}$ of Cu-CoPc-2 reached 313 mA cm^{-2} , whereas the $j_{C_2H_4}$ of Cu-CoPc-1, Cu-CoPc-3, and Cu-CoPc-4 were 220, 282, and 184 mA cm^{-2} , respectively. Notably, the catalytic performance of Cu-CoPc-2 was comparable to those of the state-of-the-art tandem catalysts up to date (Supplementary Table 3). The durability test for Cu-CoPc-2 was conducted at applied j of 480 mA cm^{-2} for 20 h. Cu-CoPc-2 exhibited around 16% decay for $FE_{C_2H_4}$ and 5% ascent for cathodic potential (Fig. 4d). The degradation of the catalytic performance was mainly attributed to the destruction of the carbon black layers and the transformation of hydrophobic surface into hydrophilic surface (Supplementary Fig. 16).

To explore the effect of CoPc on the intrinsic activity for the formation of C_2H_4 , we evaluate the ECSAs *via* Pb under potential deposition (UPD) measurements. As shown in Supplementary Fig. 17 and Supplementary Table 4, the four Cu-CoPc catalysts exhibited similar electrochemical surface areas (ECSAs) with the GDE of Cu. Nevertheless, all of the tandem catalysts exhibited higher $FE_{C_2H_4}$ and $j_{C_2H_4}$ than the GDE of Cu (35% for $FE_{C_2H_4}$, 165 mA cm^{-2} for $j_{C_2H_4}$) at applied j of 480 mA cm^{-2} . As such, the enhancement of $FE_{C_2H_4}$ was attributed to the tandem process between CoPc and Cu. As shown in Supplementary Fig. 18, the FE_{CO} for all of Cu-CoPc was higher than that for the GDE of Cu at the same applied j . Meanwhile, the FE_{CO} increased with the increased molar ratios of CoPc to Cu, indicating that CoPc served as CO-generating component. The FE_{HCOO^-} decreased with the increased molar ratios of CoPc to Cu, further revealing that the introduction of CoPc into Cu weakened the competing 2e process on Cu (Supplementary Fig. 19). Hence, the introduction of CoPc modulated the local coverage of *CO on the surface of Cu, regulating the catalytic activity for C_2^+ products towards CO_2 electroreduction.

To gain deeper insight into the tandem mechanism between Cu and CoPc, we carried out *in-situ* Raman spectroscopy measurements. Fig. 5, a and b show the *in-situ* Raman spectra towards CO_2 electroreduction over the GDE of Cu and Cu-CoPc-2. The peaks at 2037 and 2085 cm^{-1} were observed for

both the GDE of Cu and Cu-CoPc-2, which were assigned to the intramolecular stretching of the sparse and local-enrichment ^{13}CO , respectively.^[29,44] As shown in Supplementary Fig. 20, no obvious peaks associated with the intramolecular stretching of ^{13}CO was observed for CoPc, indicating that CoPc served as CO-generating component with weak ^{13}CO adsorption. As such, the peaks at 2037 and 2085 cm^{-1} for both the GDE of Cu and Cu-CoPc-2 were attributed to the intramolecular stretching of ^{13}CO on Cu sites. At each applied potential, Cu-CoPc-2 always exhibited a higher peak intensity for the intramolecular stretching of ^{13}CO in comparison with the GDE of Cu, indicating that the introduction of CoPc increased the coverage of ^{13}CO on the surface of Cu. Moreover, the peak-area ratios for the local-enrichment ^{13}CO to the sparse ^{13}CO increased from 0.66 to 2.01 when the applied potential increased from -0.4 to -0.8 V vs RHE, further revealing that the surface coverage of ^{13}CO around Cu increased at high overpotential over Cu-CoPc-2. Hence, the increased surface coverage of ^{13}CO around Cu facilitated C-C coupling, improving the catalytic activity for C_{2+} products at high overpotential over Cu-CoPc-2. These results were in good agreement with the tendency of catalytic performance. Accordingly, the tandem process between CoPc and Cu was responsible for the enhanced activity for C_{2+} products.

Discussion

In summary, we unraveled that the moderate surface coverage of ^{13}CO was beneficial for the electroreduction of CO_2 into C_2H_4 using the co-feeding gases of CO_2 and CO on the GDE of Cu. The cross-coupling process between CO_2 and CO was proved to be responsible for the enhanced activity of C_2H_4 according to isotopic labeling experiments. In addition, the tandem mechanism was further verified *via* constructing tandem catalysts of CoPc on Cu, in which Cu-CoPc-2 exhibited one-fold enhancement for the activity of C_2H_4 relative to Cu. *In-situ* Raman measurements further revealed that CO generated by CoPc increased the coverage of ^{13}CO on the surface of Cu, facilitating the process of C-C coupling. This work provided an insight into the tandem mechanism to design highly efficient catalysts towards CO_2 electroreduction into C_{2+} products.

Methods

Chemicals and materials

Potassium hydroxide (KOH, >85%), Absolute ethanol (EtOH, 99.7%), Absolute methanol (MeOH, 99.5%), Perchloric acid (HClO_4 , 70%), Lead chloride (PbCl_2 , 99.9%), Potassium chloride (KCl, 99.8%), and Carbon black (Vulcan XC-72) were purchased from Sinopharm Chemical Reagent Co. Ltd.. Cobalt(II) phthalocyanine (CoPc, 97%), 1-Propanesulfonic acid 3-(trimethylsilyl) sodium salt (DSS), (Methyl sulfoxide)- d_6 ($\text{DMSO}-d_6$), Nafion solution (5 wt%), and Nafion 115 membrane were purchased from Sigma-Aldrich. Cu disk (99.995%, ϕ 50.8 \times 3, mm) was purchased from Zhongnuo Advanced Material. $^{13}\text{CO}_2$ (99.99%) was purchased from Wuhan Newradar special gas Co. Ltd.. The deionized water was

produced using a Millipore Milli-Q grade with a resistivity of 18.2 MΩ cm. All the chemicals were used as received without any further purification.

Preparation for the GDE of Cu

In the typical preparation for the GDE of Cu, Cu disk and PTFE frame were used as target material and substrates, respectively. The sputtering was conducted *via* direct current magnetron-sputtering methods with sputtering current of 60 mA at room temperature under Ar atmosphere (2.4×10^{-3} mbar, 20 SCCM) for 1 h.

Preparation of Cu-CoPc tandem catalysts

2.0 mg of CoPc was dissolved in 20.0 mL of MeOH to form a homogeneous solution. 1.5, 3.0, 5.0, and 8.0 mL of the solution were sprayed on the GDE of Cu with geometric area of $2.0 \times 2.0 \text{ cm}^2$ to prepare Cu-CoPc-1, Cu-CoPc-2, Cu-CoPc-3, and Cu-CoPc-4, respectively.

Treatment of the GDE with Carbon black

4.0 mg of carbon black was dispersed in the mixed solution containing 1.5 mL of EtOH, 0.4 mL of H₂O, and 0.1 mL of Nafion solution *via* sonication for 30 min. Typically, 0.2 mL of dispersion was uniformly sprayed on the GDE with geometric area of $2.0 \times 2.0 \text{ cm}^2$. The prepared GDE were used as working electrodes.

Electrochemical measurements

The catalytic performances for the GDE of Cu and four Cu-CoPc tandem catalysts were carried out in a flow-cell system, in which anodic and cathodic electrolyte were wriggled by peristaltic pump with the flow rate of 5.0 mL min^{-1} and separated by Nafion 115 membrane. The nickel foam and Ag/AgCl electrodes were used as the counter electrode and reference electrode, respectively. The chronopotentiometric electrolysis was controlled by an Autolab potentiostat/galvanostat (CHI1140E). All potentials were measured *versus* the Ag/AgCl reference electrode (*vs* Ag/AgCl) and converted to the reversible hydrogen electrode reference scale (*vs* RHE) on account of the equation: $E(\text{vs RHE}) = E(\text{vs Ag/AgCl}) + 0.21 \text{ V} + 0.0591 \times \text{pH}$. The applied potential was *iR*-corrected using voltage drop from the resistance of electrolyte.

During CO₂ electroreduction, the gaseous products were monitored by an online GC equipped with a flame ionization detector (FID) and thermal conductivity detector (TCD) once every five minutes. The

liquid products were detected by ^1H NMR. Specifically, 0.4 mL of KOH solution was mixed with 0.1 mL of DMSO- d_6 . 0.1 mL of 6.0 mM DSS solution was added as an internal standard. The ^1H NMR spectra were measured on a Bruker 400 MHz NMR spectrometer.

Pb UPD was conducted in a mixed solution containing 100 mM of HClO_4 , 0.5 mM of PbCl_2 , and 50 mM of KCl. The five electrodes with geometric area of $1.0 \times 1.0 \text{ cm}^2$ were held at $-0.375 \text{ V vs Ag/AgCl}$ for 10 min in the mixed solution. The stripping of Pb was conducted *via* cyclic voltammetry (CV) sweeping from -0.25 to 0.15 V vs RHE with scan rate of 10 mV s^{-1} . The calculations of ECSAs assume the coverage of adsorbed Pb monolayer over Cu catalysts with $2e$ transfer for the oxidation of a Pb atom. According to previously reported literature, the conversion factor was $310 \mu\text{C cm}^{-2}$ for Pb UPD²⁵.

Instrumentations

SEM images were obtained with a scanning electron microscope (SEM, JSM-6700F) operated at 5 kV. HAADF-STEM images were carried out on a JEOL ARM-200F field-emission transmission electron microscope operating at an accelerating voltage of 200 kV using Mo-based TEM grids. Cu *LMM* Auger spectroscopy were performed on a VG ESCALAB MK II X-ray photoelectron spectrometer with an exciting source of Mg $K\alpha = 1253.6 \text{ eV}$. Contact angles were conducted on Attension Theta (Biolin Scientific) with 1 M KOH as droplet. The gaseous products of CO_2 electroreduction were monitored by an online GC (SHIMADZU, GC-2014). Liquid products were examined on a Varian 400 MHz NMR spectrometer (Bruker AVANCE AV III 400). Isotopic gases were detected by GC-MS (Agilent Technologies, GC7890A and MS5973C). The X-ray absorption fine structure (XAFS) spectra of Cu $K (E_0 = 8979 \text{ eV})$ edge was performed at BL14W1 beamline of Shanghai Synchrotron Radiation Facility (SSRF) operated at 3.5 GeV under “top-up” mode with a constant current of 220 mA. The XAFS data were recorded under transmission mode. The energy was calibrated accordingly to the absorption edge of pure Cu foil. Athena code was used to extract the data and fit the profiles. For XANES, the experimental absorption coefficients as function of energies $\mu(E)$ were processed by background subtraction and normalization procedures, and reported as “normalized absorption” to compare with Cu foil (Cu^0) and Cu_2O (Cu^{1+}). The Raman spectra of the samples were obtained using a LABRAMHR Raman spectrometer with an excitation wavelength of 532 nm. The *in-situ* Raman spectra towards CO_2 electroreduction were obtained using a LABRAMHR Raman spectrometer with an excitation wavelength of 785 nm.

Declarations

Acknowledgements

This work was supported by National Science Fund for Distinguished Young Scholars (21925204), National Natural Science Foundation of China (U1932146 and U19A2015), National Key Research and Development Program of China (2019YFA0405600), Key Research Program of Frontier Sciences of the

CAS (QYZDB-SSW-SLH017), Fundamental Research Funds for the Central Universities, and USTC Research Funds of the Double First-Class Initiative (YD2340002002). This work was partially carried out at the USTC Center for Micro and Nanoscale Research and Fabrication.

Author Contributions

X.K. and J.K. equally contributed to this work. Z.G., B.L, Y.H, and J.Z. conceived the idea and co-wrote the paper. X.K., J.K., and S.L. synthesized catalysts. X.K., W.Z., and C.W. conducted structural characterization. X.K., J.K., and Z.Y. performed catalytic tests. R.S. and X.K. performed XAFS measurements. All authors discussed the results and commented on the manuscript.

Additional information

Supplementary information is available in the online version of the paper. Reprints and permissions information is available online at www.nature.com/reprints. Correspondence and requests for materials should be addressed to Z.G. or J.Z..

Competing financial interests

The authors declare no competing financial interests.

References

1. Zhong, M. et al. Accelerated discovery of CO₂ electrocatalysts using active machine learning. *Nature* **581**, 178-183 (2020)
2. Choi, Y.-W., Scholten, F., Sinev, I. & Roldan Cuenya, B. Enhanced stability and CO/formate selectivity of plasma-treated SnO_x/AgO_x catalysts during CO₂ electroreduction. *J. Am. Chem. Soc.* **141**, 5261-5266 (2019).
3. Zheng, Y. et al. Understanding the roadmap for electrochemical reduction of CO₂ to multi-carbon oxygenates and hydrocarbons on copper-based catalysts. *J. Am. Chem. Soc.* **141**, 7646-7659 (2019).
4. Ross, M. B. et al. Electrocatalytic rate alignment enhances syngas generation. *Joule* **3**, 257-264 (2019).
5. Geng, Z. et al. Oxygen vacancies in ZnO nanosheets enhance CO₂ electrochemical reduction to CO. *Angew. Chem. Int. Ed.* **57**, 6054-6059 (2018).
6. Wang, L. et al. One-step reforming of CO₂ and CH₄ into high-value liquid chemicals and fuels at room temperature by plasma-driven catalysis. *Angew. Chem. Int. Ed.* **56**, 13679-13683 (2017).

7. Stroud, T. et al. Chemical CO₂ recycling via dry and bi reforming of methane using Ni-Sn/Al₂O₃ and Ni-Sn/CeO₂-Al₂O₃ catalysts. *Appl Catal B-Environ.* **224**, 125-135 (2018).
8. Sun, S., Watanabe, M., Wu, J., An, Q. & Ishihara, T. Ultrathin WO₃·0.33H₂O nanotubes for CO₂ photoreduction to acetate with high selectivity. *J. Am. Chem. Soc.* **140**, 6474-6482 (2018).
9. Rao, H., Schmidt, L. C., Bonin, J. & Robert, M. Visible-light-driven methane formation from CO₂ with a molecular iron catalyst. *Nature* **548**, 74-77 (2017).
10. Bond, G. M. et al. Development of integrated system for biomimetic CO₂ sequestration using the enzyme carbonic anhydrase. *Energy Fuels* **15**, 309-316 (2001).
11. Zhang, H. et al. Bacteria photosensitized by intracellular gold nanoclusters for solar fuel production. *Nat. Nanotechnol.* **13**, 900-905 (2018).
12. Yang, F. et al. Highly efficient CO₂ electroreduction on ZnN₄-based single-atom catalyst *Angew. Chem. Int. Ed.* **57**, 12303-12307 (2018).
13. Verma, S., Lu, S. & Kenis, P. J. A. Co-electrolysis of CO₂ and glycerol as a pathway to carbon chemicals with improved technoconomics due to low electricity consumption. *Nat. Energy* **4**, 466-474 (2019).
14. Wu, Y., Jiang, Zhan., Lu, Xu., Liang, Y. & Wang, H. Domino electroreduction of CO₂ to methanol on a molecular catalyst. *Nature* **575**, 639-642 (2019).
15. Wang, Y. et al. Catalyst synthesis under CO₂ electroreduction favours faceting and promotes renewable fuels electrosynthesis. *Nat. Catal.* **3**, 98-106 (2020).
16. Luc, W. et al. SO₂-induced selectivity change in CO₂ electroreduction. *J. Am. Chem. Soc.* **141**, 9902-9909 (2019).
17. Jiang, K. et al. Metal ion cycling of Cu foil for selective C-C coupling in electrochemical CO₂ reduction. *Nat. Catal.* **1**, 111-119 (2018).
18. Hoang, T. T. H. et al. Nanoporous copper-silver alloys by additive-controlled electrodeposition for the selective electroreduction of CO₂ to ethylene and ethanol. *J. Am. Chem. Soc.* **140**, 5791-5797 (2018).
19. Kang, P., Chen, Z., Nayak, A., Zhang, S. & Meyer, T. J. Single catalyst electrocatalytic reduction of CO₂ in water to H₂+CO syngas mixtures with water oxidation to O₂. *Energy Environ. Sci.* **7**, 4007-4012 (2014).
20. Wang, M. et al. CO₂ electrochemical catalytic reduction with a highly active cobalt phthalocyanine. *Nat. Commun.* **10**, 3602 (2019).
21. Lin, L. et al. Synergistic catalysis over iron-nitrogen sites anchored with cobalt phthalocyanine for efficient CO₂ electroreduction. *Adv. Mater.* **31**, 1903470 (2019).
22. Li, F. et al. Cooperative CO₂-to-ethanol conversion via enriched intermediates at molecule-metal catalyst interfaces. *Nat. Catal.* **3**, 75-82 (2020).
23. Jung, H. et al. Electrochemical fragmentation of Cu₂O nanoparticles enhancing selective C-C coupling from CO₂ reduction reaction. *J. Am. Chem. Soc.* **141**, 4624-4633 (2019).

24. Luc, W. et al. Two-dimensional copper nanosheets for electrochemical reduction of carbon monoxide to acetate. *Nat. Catal.* **2**, 423-430 (2019).
25. Gao, J. et al. Selective C-C coupling in carbon dioxide electroreduction via efficient spillover of intermediates as supported by operando Raman spectroscopy. *J. Am. Chem. Soc.* **141**, 18704-18714 (2019).
26. Lum, Y. & Ager, J. W. Evidence for product-specific active sites on oxide-derived Cu catalysts for electrochemical CO₂ reduction. *Nat. Catal.* **2**, 86-93 (2019).
27. Zhou, Y. et al. Dopant-induced electron localization drives CO₂ reduction to C₂ hydrocarbons. *Nat. Chem.* **10**, 974-980 (2018).
28. Arán-Ais, R. M., Scholten, F., Kunze, S., Rizo, R. & Roldan Cuenya, B. The role of in situ generated morphological motifs and Cu(I) species in C₂₊ product selectivity during CO₂ pulsed electroreduction. *Nat. Energy* **5**, 317-325 (2020).
29. Li, Y. C. et al. Binding site diversity promotes CO₂ electroreduction to ethanol. *J. Am. Chem. Soc.* **141**, 8584-8591 (2019).
30. Yang, D. et al. Selective electroreduction of carbon dioxide to methanol on copper selenide nanocatalysts. *Nat. Commun.* **10**, 677 (2019).
31. Higgins, D. et al. Guiding electrochemical carbon dioxide reduction toward carbonyls using copper silver thin films with interphase miscibility. *ACS Energy Lett.* **3**, 2947-2955 (2018).
32. Clark, E. L., Hahn, C., Jaramillo, T. F. & Bell, A. T. Electrochemical CO₂ reduction over compressively strained CuAg surface alloys with enhanced multi-carbon oxygenate selectivity. *J. Am. Chem. Soc.* **139**, 15848-15857 (2017).
33. Ren, D., Ang, B. S.-H., & Yeo, B. S. Tuning the selectivity of carbon dioxide electroreduction toward ethanol on oxide-derived Cu_xZn catalysts. *ACS Catal.* **6**, 8239-8247 (2016).
34. Lee, S., Park, G. & Lee, J. Importance of Ag-Cu biphasic boundaries for selective electrochemical reduction of CO₂ to ethanol. *ACS Catal.* **7**, 8594-8604 (2017).
35. Morales-Guio, C. G. et al. Improved CO₂ reduction activity towards C₂₊ alcohols on a tandem gold on copper electrocatalyst. *Nat. Catal.* **1**, 764-771 (2018).
36. Lum, Y. & Ager, J. W. Sequential catalysis controls selectivity in electrochemical CO₂ reduction on Cu. *Energy Environ. Sci.* **11**, 2935-2944 (2018).
37. Wang, X. et al. Mechanistic reaction pathways of enhanced ethylene yields during electroreduction of CO₂-CO co-feeds on Cu and Cu-tandem electrocatalysts. *Nat. Nanotech.* **14**, 1063-1070 (2019).
38. Ren, D. et al. Atomic layer deposition of ZnO on CuO enables selective and efficient electroreduction of carbon dioxide to liquid fuels. *Angew. Chem. Int. Ed.* **58**, 15036-15040 (2019).
39. Wakerley, D. et al. Bio-inspired hydrophobicity promotes CO₂ reduction on a Cu surface. *Nat. Mater.* **18**, 1222-1227 (2019).

40. Dinh, C.-T. et al. CO₂ electroreduction to ethylene via hydroxide-mediated copper catalysis at an abrupt interface. *Science* **360**, 783-787 (2018).
41. Li, J. et al. Efficient electrocatalytic CO₂ reduction on a three-phase interface. *Nat. Catal.* **1**, 592-600 (2018).
42. Sandberg, R. B., Montoya, J. H., Chan, K. & Nørskov, J. K. CO-CO coupling on Cu facets: coverage, strain and field effects. *Surf. Sci.* **654**, 56-62 (2016).
43. Ren, S. et al. Molecular electrocatalysts can mediate fast, selective CO₂ reduction in a flow cell. *Science* **365**, 367-369 (2019).
44. Gunathunge, C. M. et al. Spectroscopic observation of reversible surface reconstruction of copper electrodes under CO₂ reduction. *J. Phys. Chem. C* **121**, 12337-12344 (2017).

Figures

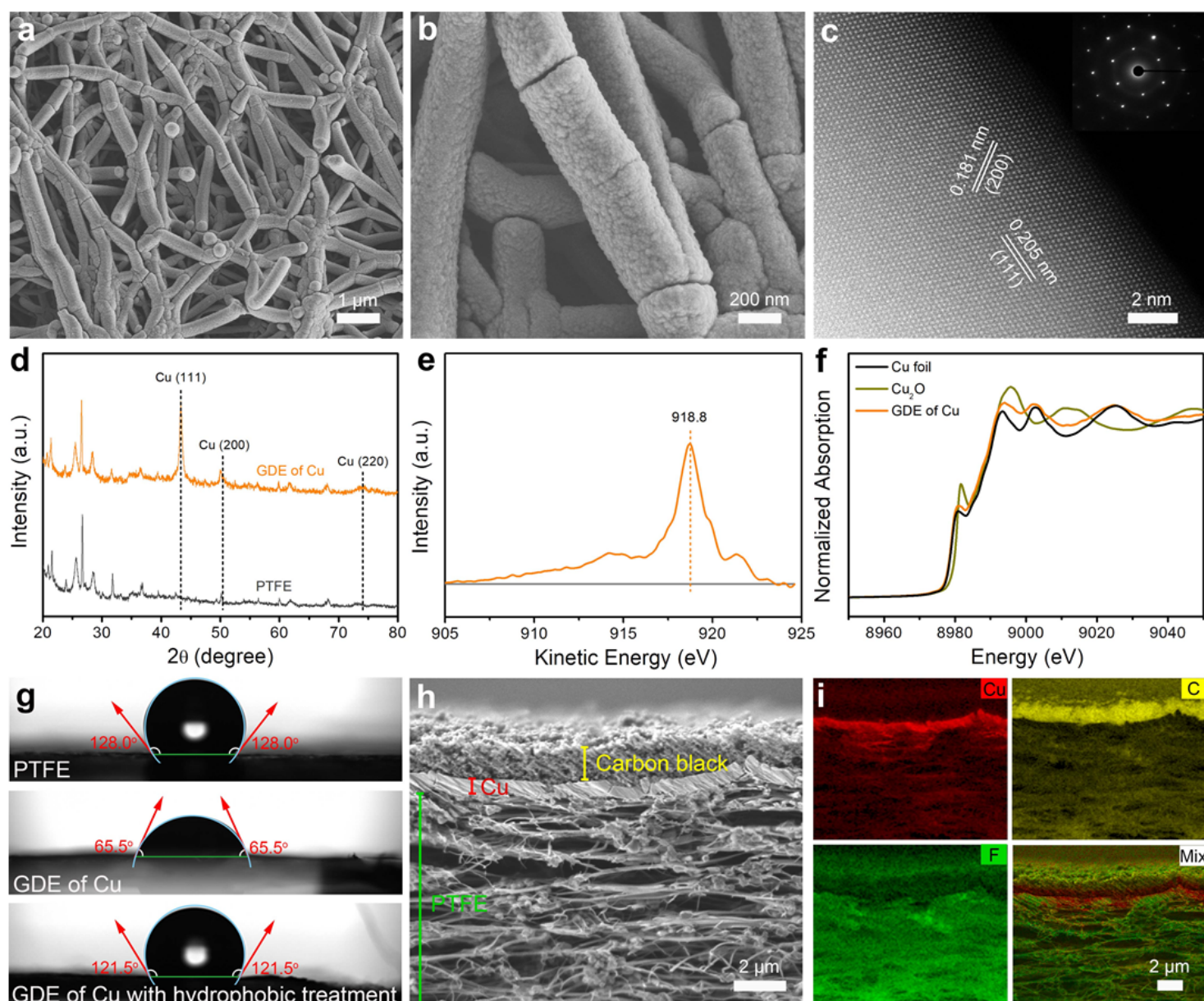


Figure 1

Structural characterization for the GDE of Cu. a,b, SEM images for the GDE of Cu. c, HAADF-STEM image of Cu nanocrystal. The inset shows the corresponding SAED pattern. d, XRD patterns for PTFE and GDE of Cu. e, Cu LMM spectrum for the GDE of Cu. f, XANES spectra of Cu foil, Cu₂O, and GDE of Cu. g, Contact angles of PTFE, GDE of Cu, and GDE of Cu with hydrophobic treatment. h,i, The SEM image (h) and EDX elemental mapping (i) of cross-sectional GDE of Cu with hydrophobic treatment.

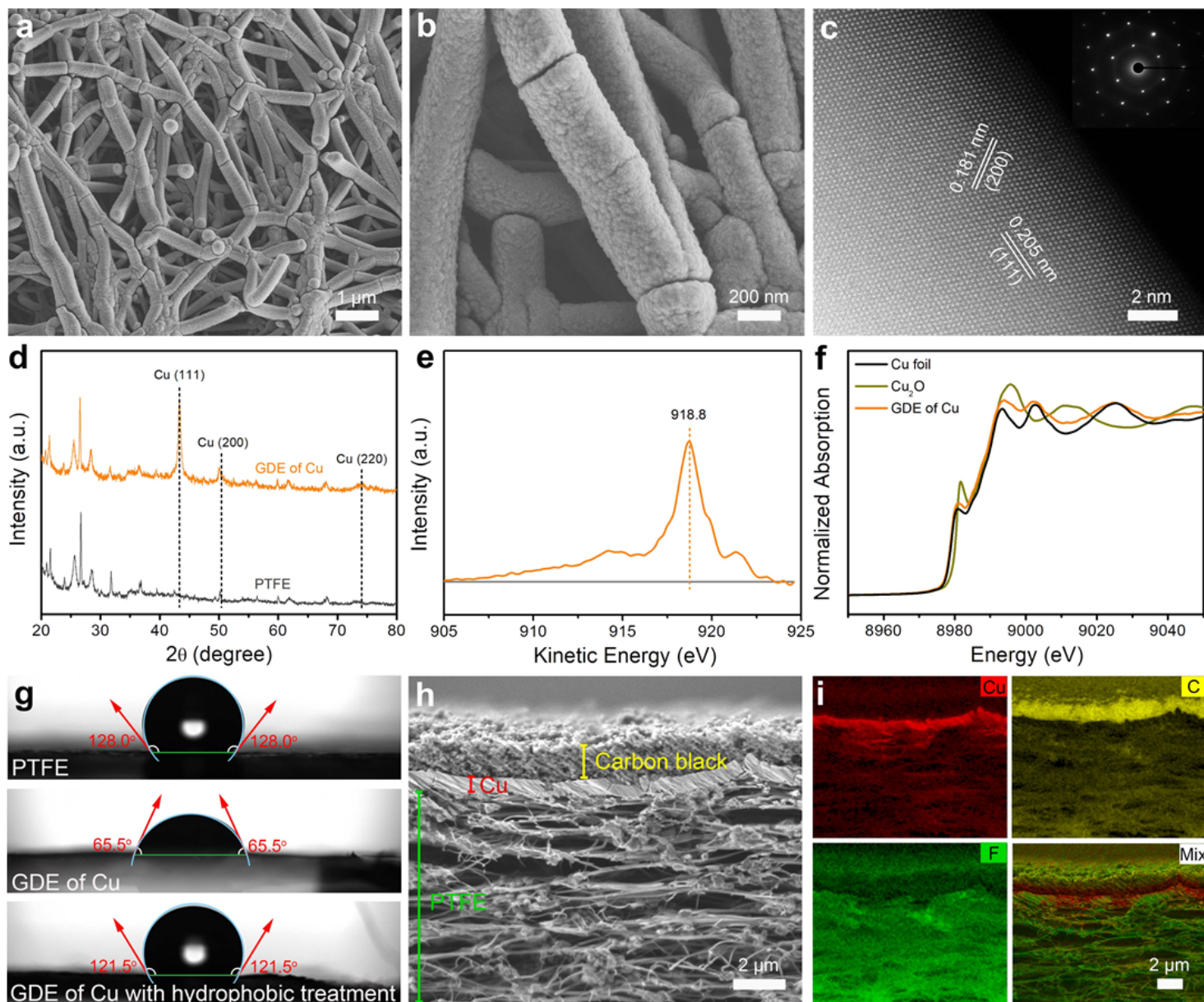


Figure 1

Structural characterization for the GDE of Cu. a,b, SEM images for the GDE of Cu. c, HAADF-STEM image of Cu nanocrystal. The inset shows the corresponding SAED pattern. d, XRD patterns for PTFE and GDE of Cu. e, Cu LMM spectrum for the GDE of Cu. f, XANES spectra of Cu foil, Cu₂O, and GDE of Cu. g, Contact angles of PTFE, GDE of Cu, and GDE of Cu with hydrophobic treatment. h,i, The SEM image (h) and EDX elemental mapping (i) of cross-sectional GDE of Cu with hydrophobic treatment.

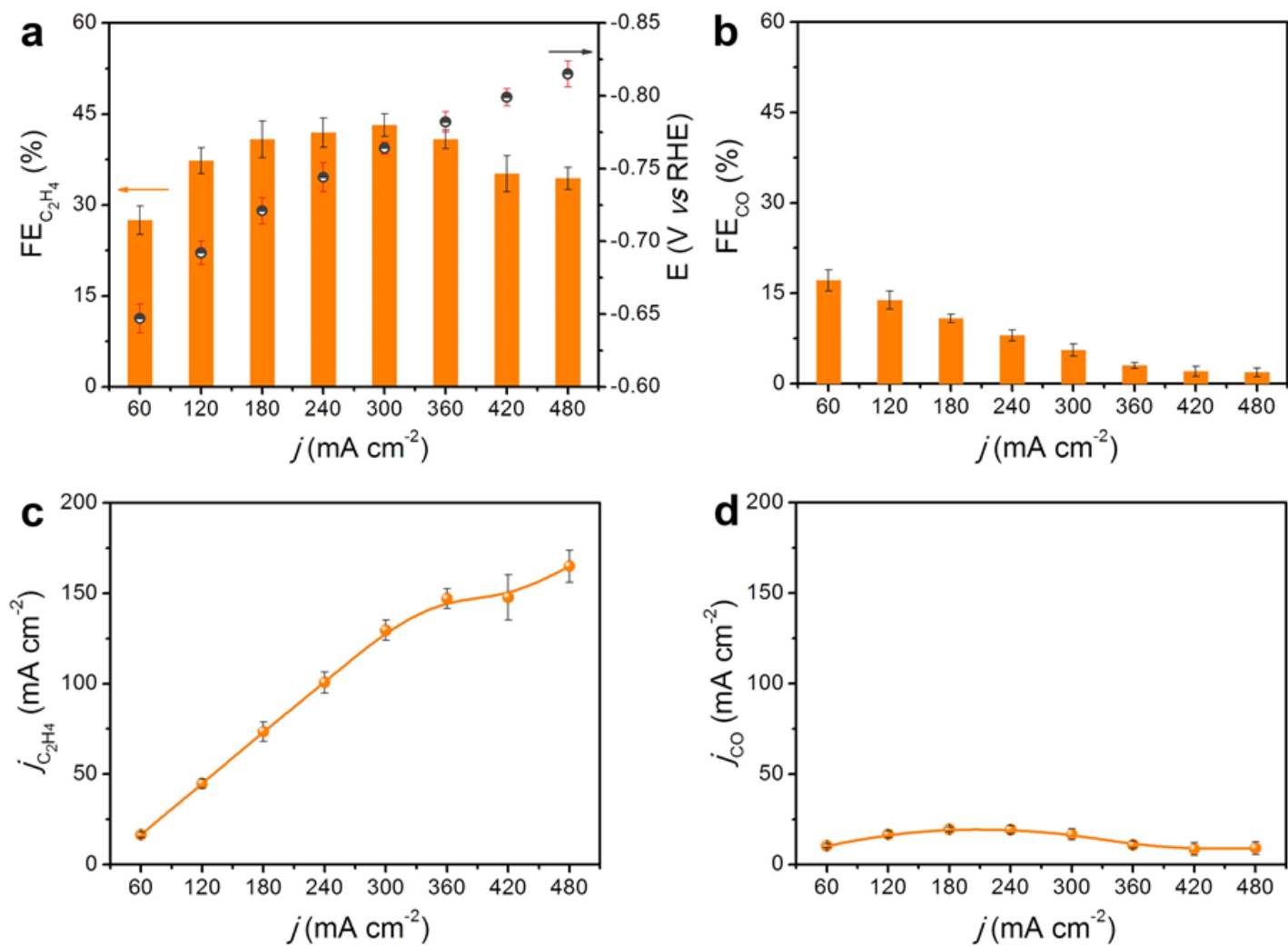


Figure 2

Catalytic performance for the GDE of Cu towards CO₂ electroreduction. a,b,c,d, FE_{C₂H₄} (a), FE_{CO} (b), $j_{C_2H_4}$ (c), and j_{CO} (d) for the GDE of Cu. Scale bar represents the standard deviations for the three separated tests. The applied potential was iR-corrected using voltage drop from the resistance of electrolyte.

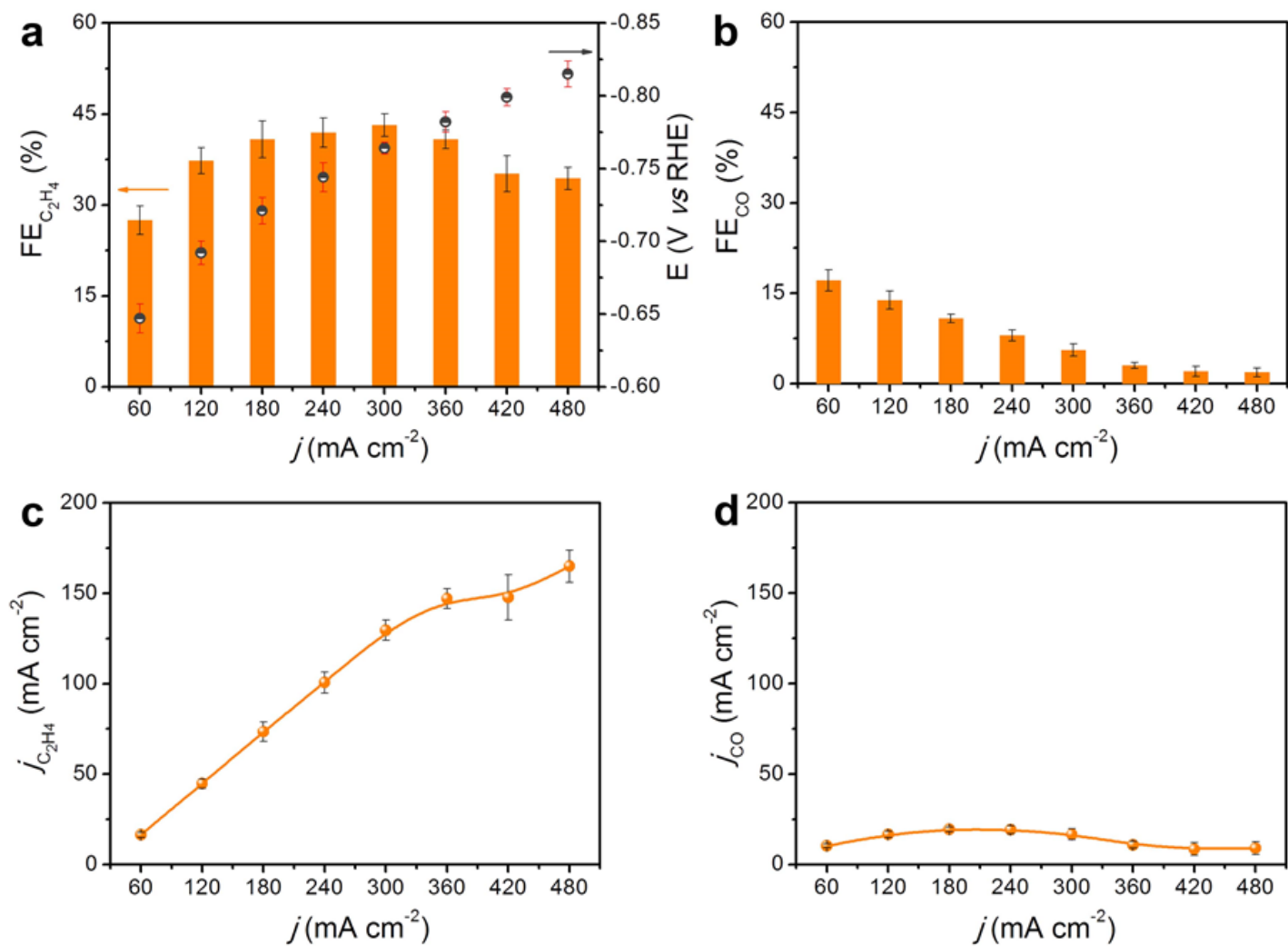


Figure 2

Catalytic performance for the GDE of Cu towards CO₂ electroreduction. a,b,c,d, FE_{C₂H₄} (a), FE_{CO} (b), $j_{C_2H_4}$ (c), and j_{CO} (d) for the GDE of Cu. Scale bar represents the standard deviations for the three separated tests. The applied potential was iR-corrected using voltage drop from the resistance of electrolyte.

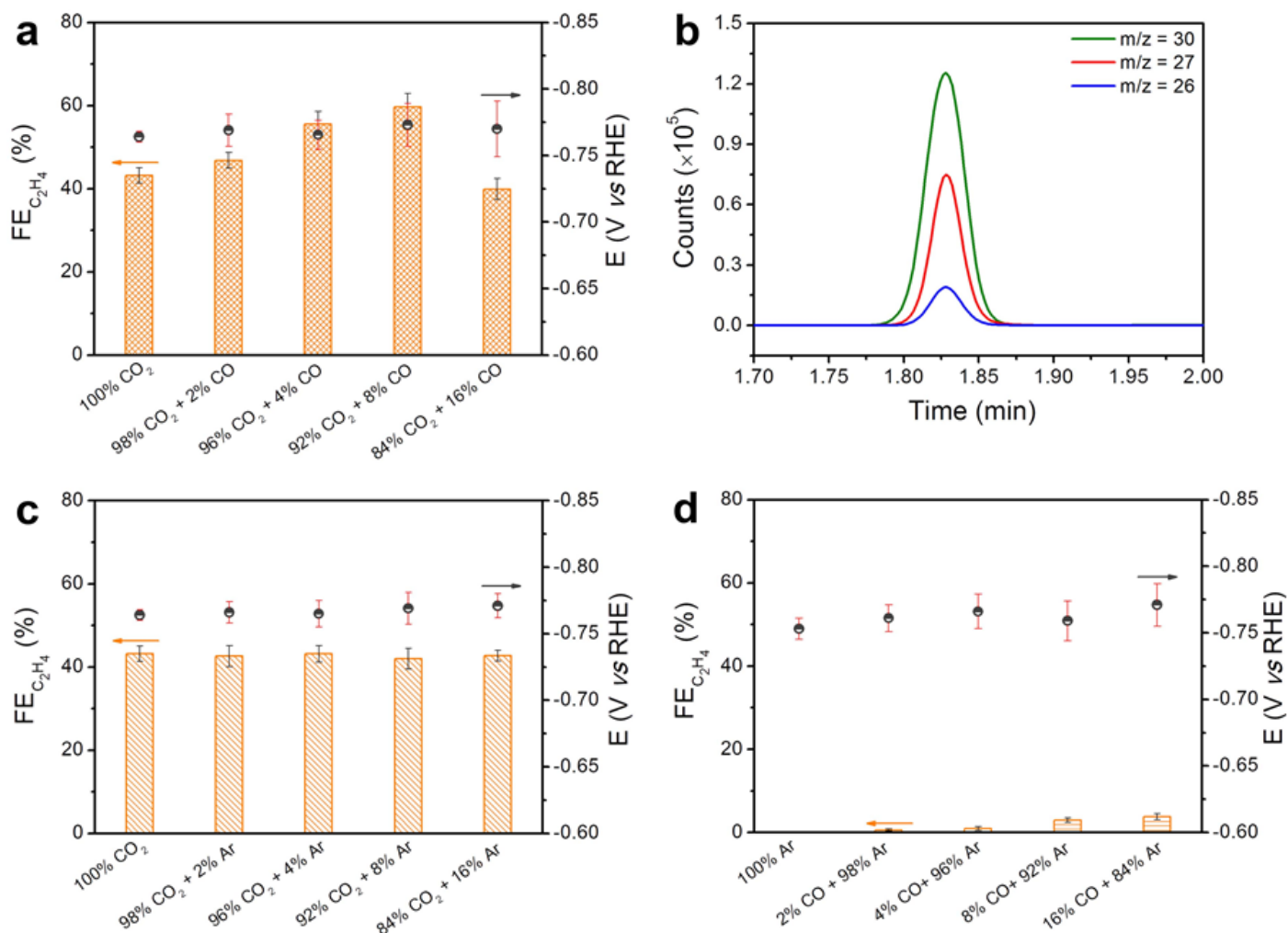


Figure 3

Tandem mechanism for the GDE of Cu. a, FE_{C₂H₄} for the GDE of Cu using various co-feeding gases of CO₂ with CO. b, The mass spectra of the C₂H₄-correlated fragments with m/z of 30, 27, and 26 during electrolyzing co-feeding gases of ¹³CO₂ and CO with molar ratio of 92:8 for the GDE of Cu at applied j of 300 mA cm⁻². c, d, FE_{C₂H₄} for the GDE of Cu using various co-feeding gases of CO₂ with Ar (c) and CO with Ar (d) at applied j of 300 mA cm⁻². Scale bar represents the standard deviations for the three separated tests. The applied potential was iR-corrected using voltage drop from the resistance of electrolyte.

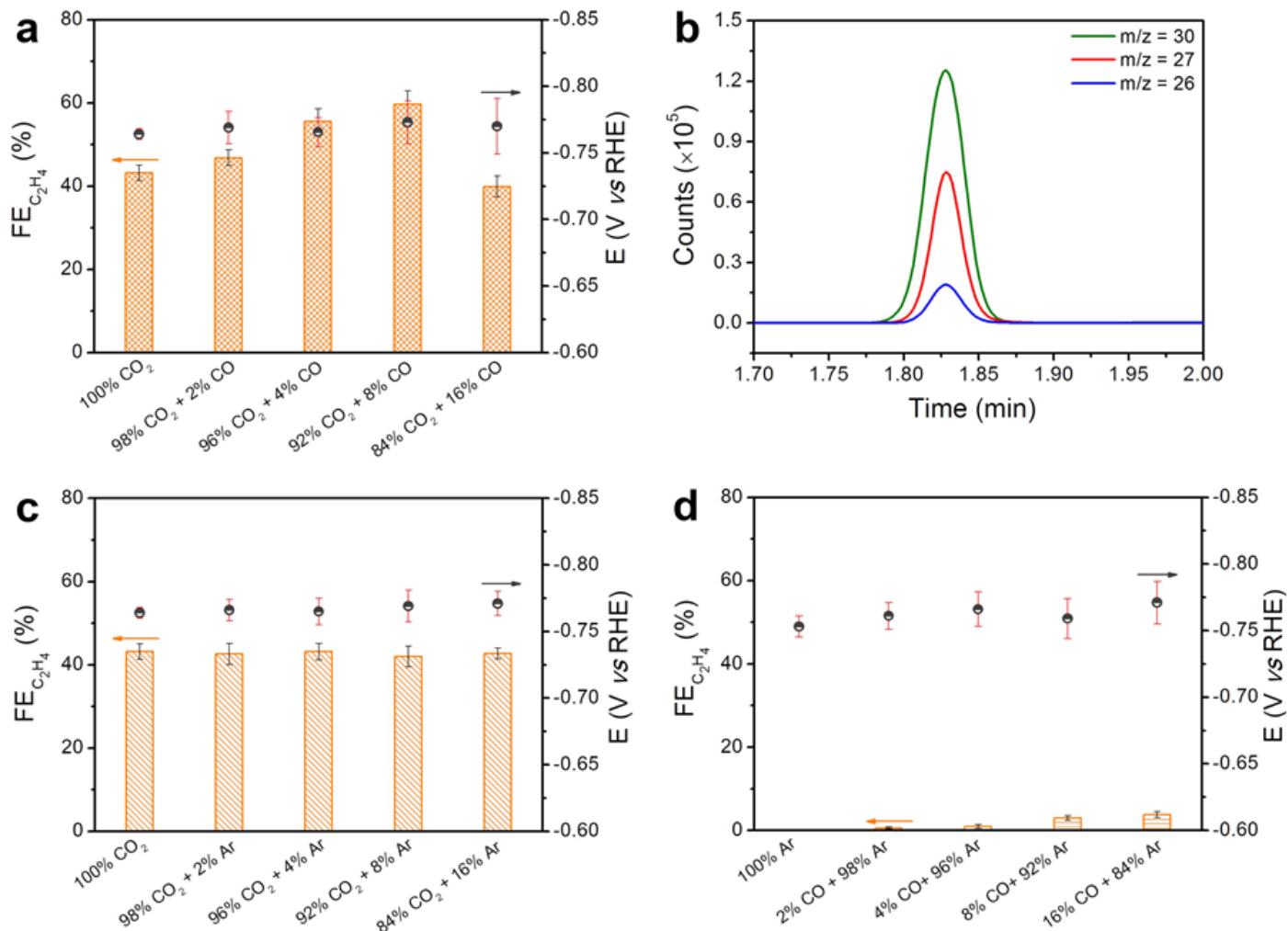


Figure 3

Tandem mechanism for the GDE of Cu. a, FE_{C₂H₄} for the GDE of Cu using various co-feeding gases of CO₂ with CO. b, The mass spectra of the C₂H₄-correlated fragments with m/z of 30, 27, and 26 during electrolyzing co-feeding gases of ¹³CO₂ and CO with molar ratio of 92:8 for the GDE of Cu at applied j of 300 mA cm⁻². c, d, FE_{C₂H₄} for the GDE of Cu using various co-feeding gases of CO₂ with Ar (c) and CO with Ar (d) at applied j of 300 mA cm⁻². Scale bar represents the standard deviations for the three separated tests. The applied potential was iR-corrected using voltage drop from the resistance of electrolyte.

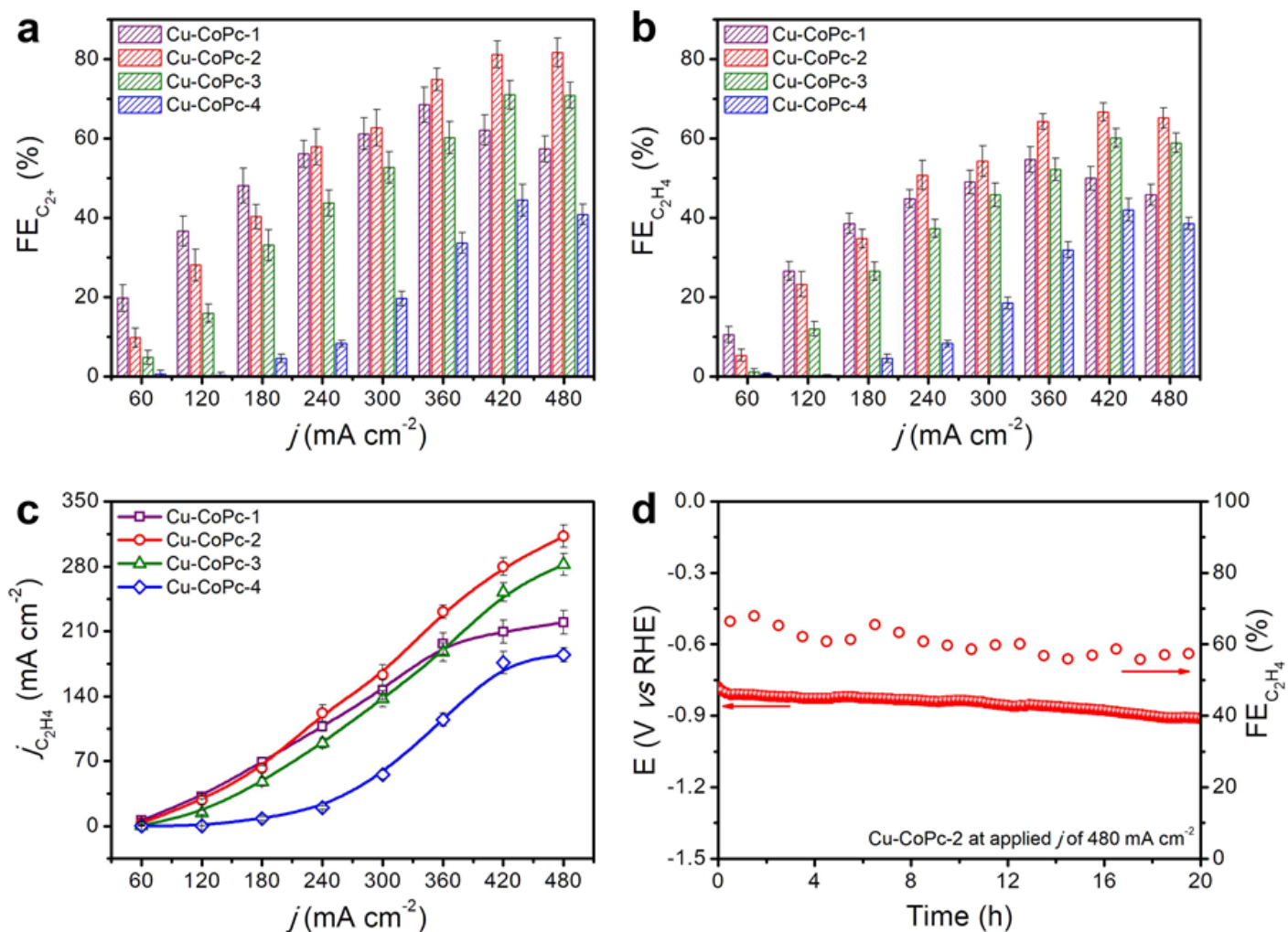


Figure 4

Catalytic performance of Cu-CoPc tandem catalysts. a, FE_{C₂⁺} for the four Cu-CoPc catalysts. b,c, FE_{C₂H₄} (b) and j_{C₂H₄} (c) for the four Cu-CoPc catalysts. d, 20-h durability tests for Cu-CoPc-2. Scale bar represents the standard deviations for the three separated tests. The applied potential was iR-corrected using voltage drop from the resistance of electrolyte.

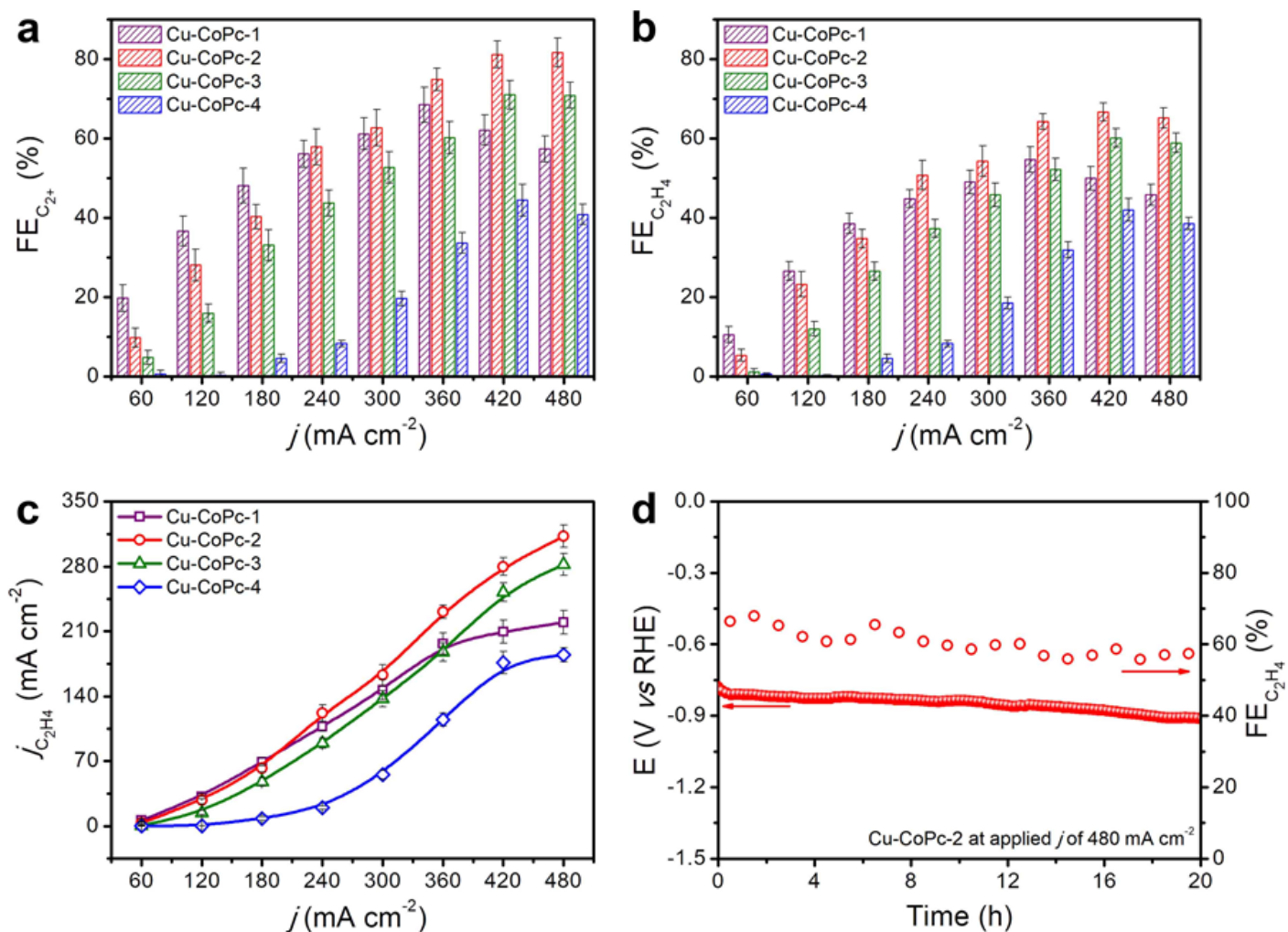


Figure 4

Catalytic performance of Cu-CoPc tandem catalysts. a, $FE_{C_2^+}$ for the four Cu-CoPc catalysts. b,c, $FE_{C_2H_4}$ (b) and $j_{C_2H_4}$ (c) for the four Cu-CoPc catalysts. d, 20-h durability tests for Cu-CoPc-2. Scale bar represents the standard deviations for the three separated tests. The applied potential was iR-corrected using voltage drop from the resistance of electrolyte.

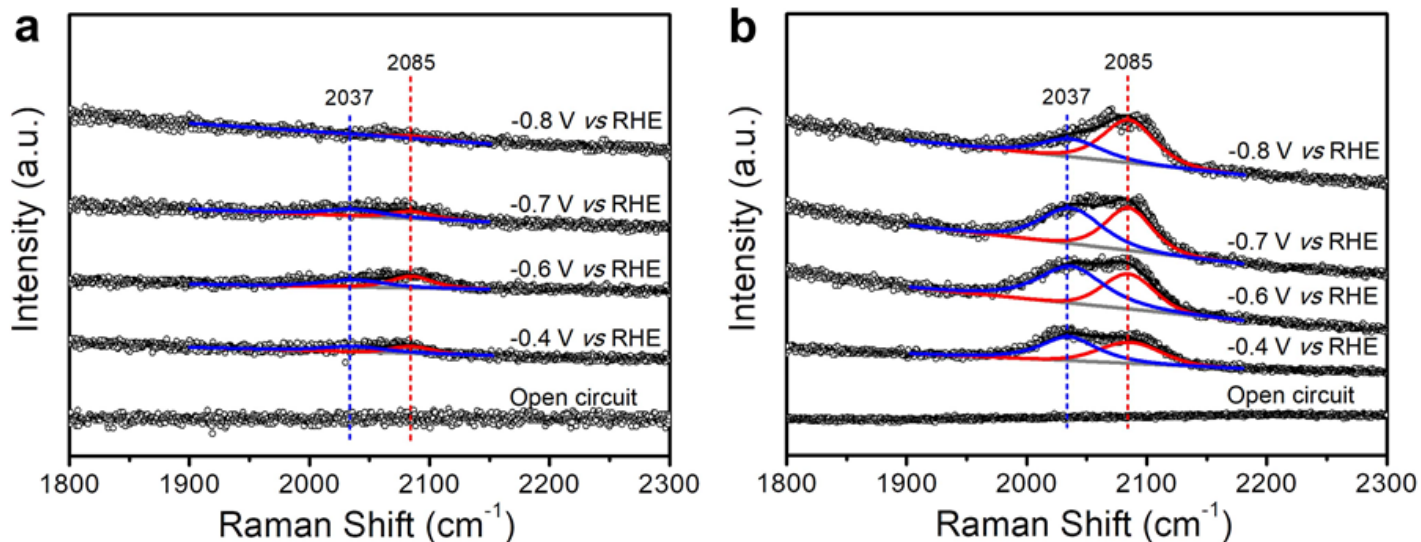


Figure 5

In-situ Raman spectroscopy towards CO₂ electroreduction. a,b, In-situ Raman spectra towards CO₂ electroreduction over the GDE of Cu (a) and Cu-CoPc-2 (b) at different applied potential.

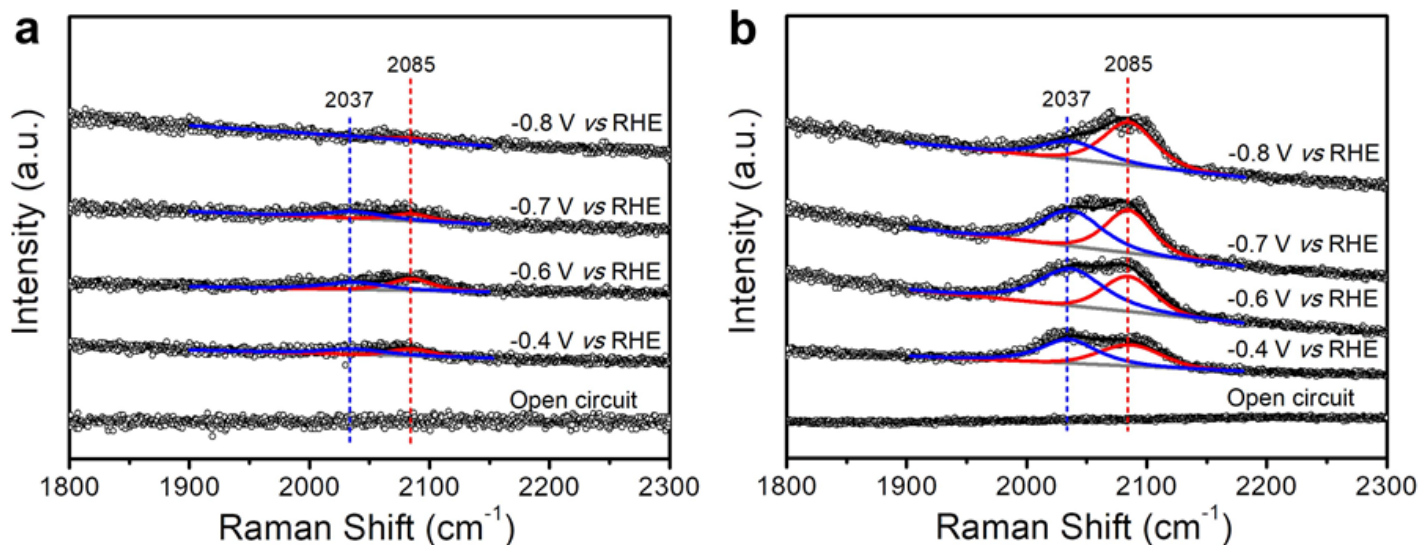


Figure 5

In-situ Raman spectroscopy towards CO₂ electroreduction. a,b, In-situ Raman spectra towards CO₂ electroreduction over the GDE of Cu (a) and Cu-CoPc-2 (b) at different applied potential.

Supplementary Files

This is a list of supplementary files associated with this preprint. Click to download.

- [CCCouplingTandemMechanismCO2ReductionSI11242020.doc](#)
- [CCCouplingTandemMechanismCO2ReductionSI11242020.doc](#)
- [TOCGraphic.png](#)
- [TOCGraphic.png](#)